JGR Solid Earth

RESEARCH ARTICLE
10.1029/2022JB025681

Key Points:

- A mode separation technique is proposed to suppress near zero-time-lag noise in cross-correlation functions for ambient noise tomography
- The fine upper crustal *Vs* model reveals an apparent low-velocity belt consistent with local earthquakes beneath the Anninghe fault zone
- Scenario earthquake simulations highlight the significance of fine structures in assessing large earthquake hazards

Supporting Information:

Supporting Information may be found in the online version of this article.

Correspondence to:

H. Yao,
hjyao@ustc.edu.cn

Citation:

Luo, S., Yao, H., Wen, J., Yang, H., Tian, B., & Yan, M. (2023). Apparent low-velocity belt in the shallow Anninghe fault zone in SW China and its implications for seismotectonics and earthquake hazard assessment. *Journal of Geophysical Research: Solid Earth*, *128*, e2022JB025681. https://doi.org/10.1029/2022JB025681

Received 24 SEP 2022
Accepted 20 FEB 2023

Author Contributions:

Conceptualization: Song Luo, Huajian Yao
Data curation: Huajian Yao, Hongfeng Yang, Baofeng Tian
Formal analysis: Mengxuan Yan
Funding acquisition: Song Luo, Huajian Yao
Investigation: Song Luo, Huajian Yao, Jian Wen
Methodology: Song Luo, Huajian Yao
Project Administration: Huajian Yao
Resources: Huajian Yao
Software: Song Luo, Huajian Yao, Jian Wen
Validation: Song Luo, Jian Wen, Mengxuan Yan
Visualization: Song Luo, Jian Wen

Apparent Low-Velocity Belt in the Shallow Anninghe Fault Zone in SW China and Its Implications for Seismotectonics and Earthquake Hazard Assessment

Song Luo[1], Huajian Yao[1,2,3], Jian Wen[1], Hongfeng Yang[4,5], Baofeng Tian[6], and Mengxuan Yan[1]

[1]Laboratory of Seismology and Physics of the Earth's Interior, School of Earth and Space Sciences, University of Science and Technology of China, Hefei, China, [2]Mengcheng National Geophysical Observatory, University of Science and Technology of China, Mengcheng, China, [3]CAS Center for Excellence in Comparative Planetology, University of Science and Technology of China, Hefei, China, [4]Earth System Science Programme, Faculty of Science, The Chinese University of Hong Kong, Hong Kong, China, [5]Shenzhen Research Institute, The Chinese University of Hong Kong, Shenzhen, China, [6]Institute of Geophysics, China Earthquake Administration, Beijing, China

Abstract The Anninghe fault forms the eastern boundary of the Sichuan-Yunnan block in Southwest China and has been identified as an earthquake gap zone. This study intends to construct the upper crustal shear wave velocity (*Vs*) structure beneath the Anninghe fault to understand its seismotectonics and potential large earthquake hazards. We deployed a dense seismic array along the southern central Anninghe fault valley. From the 3-month continuous records, we calculated vertical-component cross-correlation functions (CCFs). However, the surface wave signals in the CCFs are intensely interfered by near zero-time-lag noise. We proposed a mode separation method based on the high-resolution linear Radon transform, which suppressed the interfered noise and greatly enhanced the surface wave signals for ambient noise tomography of the *Vs* structure. The fine upper crustal structure reveals a distinct narrow low-velocity belt within a depth of 3 km beneath the Anninghe fault zone. At deeper depths (4.5–8 km), the narrow low-velocity belt shifts to the east and correlates with the distribution of local earthquakes. Combining previous results with our new findings, we presented a seismotectonic model of the southern central Anninghe fault, which interprets the narrow low-velocity belt as a water-contained fracture zone that forms a seismogenic zone at deeper depths under transpression. In addition, we demonstrated through scenario earthquake simulations that fine structures play a significant role in the assessment of earthquake hazards along the Anninghe fault. As such, this study provides a typical window into seismotectonics and large earthquake hazards in the active southeastern Tibetan Plateau.

Plain Language Summary The Anninghe fault is located in Southwest China, and it has experienced a series of large earthquakes ($M \geq 7$) during its history. However, the Anninghe fault has been silent for nearly 30 years; it has been suggested that there is a high risk of large earthquakes occurring there. To investigate the deep structural background and potential earthquake hazards associated with the Anninghe fault zone, we deployed a dense seismic array along this fault zone. During data processing, we proposed a method to eliminate coherent noise and enhance the signals considerably, which is essential for the subsequent tomography of the structures underneath. The final tomographic model shows that the Anninghe fault zone has a distinctively low seismic wave speed at shallow depths and dips to the east at deeper depths. As this observation agrees with the distribution of local earthquakes and previous findings, it may indicate the existence of a seismogenic zone capable of generating earthquakes. Additionally, we further demonstrated through simulations of large earthquakes that the high-resolution model developed in this study is important for assessing earthquake hazards along the Anninghe fault.

1. Introduction

The Anninghe fault zone lies in the Sichuan-Yunnan region to the southeast of the Tibetan Plateau and is one of the most important north-south left-lateral strike-slip faults in China. During the Cenozoic, the Indian plate subducted northward beneath the Eurasian plate, resulting in the uplift of the Tibetan Plateau and the extrusion of continental material. It has been shown that crustal material rotates clockwise around the Eastern Himalayan syntaxis (e.g., Royden et al., 1997; Schoenbohm et al., 2006; Tapponnier et al., 1982; Q. Wang et al., 2001). Active faults, such as the Anninghe fault, have played a significant role in accommodating the extrusion process through large-scale strike-slip and thrust movements (e.g., Ren, 2014). These movements inevitably cause severe

Writing – original draft: Song Luo
Writing – review & editing: Song Luo, Huajian Yao, Jian Wen, Hongfeng Yang, Baofeng Tian

earthquakes. By utilizing the Anninghe fault as a window to study the upper crustal response of the extrusion process, it is possible to gain a better understanding of the seismogenic environment and large earthquake hazards associated with the active faults in the Sichuan-Yunnan area.

Numerous studies have examined the tectonic evolution, medium structure, slip rate, stress-strain state, and earthquake risk of the Anninghe fault from the perspectives of geology, geophysics, geochemistry, and geodesy. It is generally believed that the Anninghe fault originated in the Precambrian and experienced multiple episodes of compression and extension activities, resulting in the development of the Proterozoic to Mesozoic magmatic complex belt along the fault zone (e.g., Y. Chen et al., 2021). The large and thick Xigeda strata developed during the early Pleistocene due to rifting regimes, resulting in the current topography of two grabens and one base (e.g., Y. Chen et al., 2021; He & Ikeda, 2007; Ren, 2014; Y. Zhang et al., 2010). The Anninghe fault exhibits left-lateral strike-slip movement under the NW-SE maximum horizontal stress, with a horizontal strike-slip rate of 4–6 mm/a (e.g., Y. Chen et al., 2021; H. Wang et al., 2018), and a thrust component, where the west block (with respect to the Anninghe fault) is actively inserted below the east block, with a vertical velocity of approximately 0–2 mm/a (e.g., Y. Chen et al., 2021; Su et al., 2017; Tian et al., 2021; Zhu et al., 2017). Based on paleoearthquake studies, the Anninghe fault zone has experienced multiple earthquakes of magnitude 7 or higher throughout history, with a recurrence period of approximately 500–800 a (e.g., Ran et al., 2008; H. Wang, Ran, Li, & Chen, 2014; H. Wang, Ran, Li, Gomez, & Chen, 2014).

However, there have been no earthquakes of magnitude greater than or equal to 7 on the Anninghe fault since 1536, and since January 1977, the Anninghe fault has experienced a 30 yr period of quiescence without earthquakes with a magnitude greater than 4.0, forming a seismic gap, so an earthquake of a large magnitude is highly probable in the future (Wen et al., 2008). A number of other studies support this viewpoint, such as slip deficit studies based on global positioning system (GPS) data (Y. C. Li et al., 2021), interseismic coupling studies based on GPS data and interferometric synthetic aperture radar (InSAR) data (Jiang et al., 2015; Y. C. Li, Nocquet, Shan, & Jian, 2021), strain rate research based on GPS data (Q. Wang et al., 2020), seismogenic depth and seismic risk research based on seismic data and deformation data (J. Li et al., 2020), *b* value distribution studies based on seismic data (Yi et al., 2008), studies based on CO_2 and radon gas emissions (Y. Yang et al., 2018; Y. Yang et al., 2021), and earthquake hazard assessment based on rupture scenarios (Cheng et al., 2021; S. Yao & Yang, 2022).

There are many villages with dense populations along the valley of the Anninghe fault (Figure 1c). Assessing the reliable distribution of earthquake hazards caused by strong earthquakes along the Anninghe fault zone is beneficial not only for urban planning but also for people's safety. The seismic hazard of the Anninghe fault has been studied in some previous studies. For example, Cheng et al. (2021) calculated the peak ground acceleration (PGA) of the Anninghe-Zemuhe-Daliangshan area by considering multisegment ruptures and slip rates; the PGA obtained was on average higher than the China Seismic Ground Motion Parameters Zonation Map. For another example, S. Yao and Yang (2022) performed rupture simulations of the Anninghe fault by using the stress accumulation at the fault plane estimated by the interseismic locking model as the initial stress status, with the results indicating that the Anninghe fault has the potential for generating earthquakes with magnitudes of 6.9–7.3. Many factors are involved in the strong ground motion calculation caused by large earthquakes, including rupture depth, rupture size, rupture directivity, rupture geometry, initial stress state, topographic relief, and medium elastic structure (e.g., S. Yao & Yang, 2022). As part of these factors, the influence of underneath structures on the large earthquake hazards in the Anninghe fault zone has not yet been investigated.

In terms of geophysical investigations of the Anninghe fault, previous studies have mainly investigated the regional-scale tomography of surface waves and body waves (e.g., Y. Hu & Wang, 2018; Q. Y. Liu et al., 2014; W. Liu, Wu, & Zhang, 2019; Y. C. Liu et al., 2021; W. Wang et al., 2017; Z. Wang et al., 2015; Z. Zhang et al., 2020) and determined the *S* wave velocity, *P* wave velocity, and velocity ratio of the crust and upper mantle. According to these results, there are obvious anomalies of high velocity (Z. Zhang et al., 2020), high- and low-velocity boundaries (W. Liu, Wu, & Zhang, 2019), and high Poisson's ratios (W. Wang et al., 2017) in the crust near the Anninghe-Zemuhe fault. However, these large-scale structural models have a lateral resolution of more than tens of kilometers, which makes it difficult to distinguish the fine structure within the Anninghe fault zone. Several studies have presented local two-dimensional (2D) structures beneath the Anninghe fault zone (Shao et al., 2022; Wan et al., 2010; Z. Yang et al., 2011), where the Anninghe fault zone appears to be a zone of low velocity and high conductivity. However, it still lacks the constraints of the fine three-dimensional (3D)

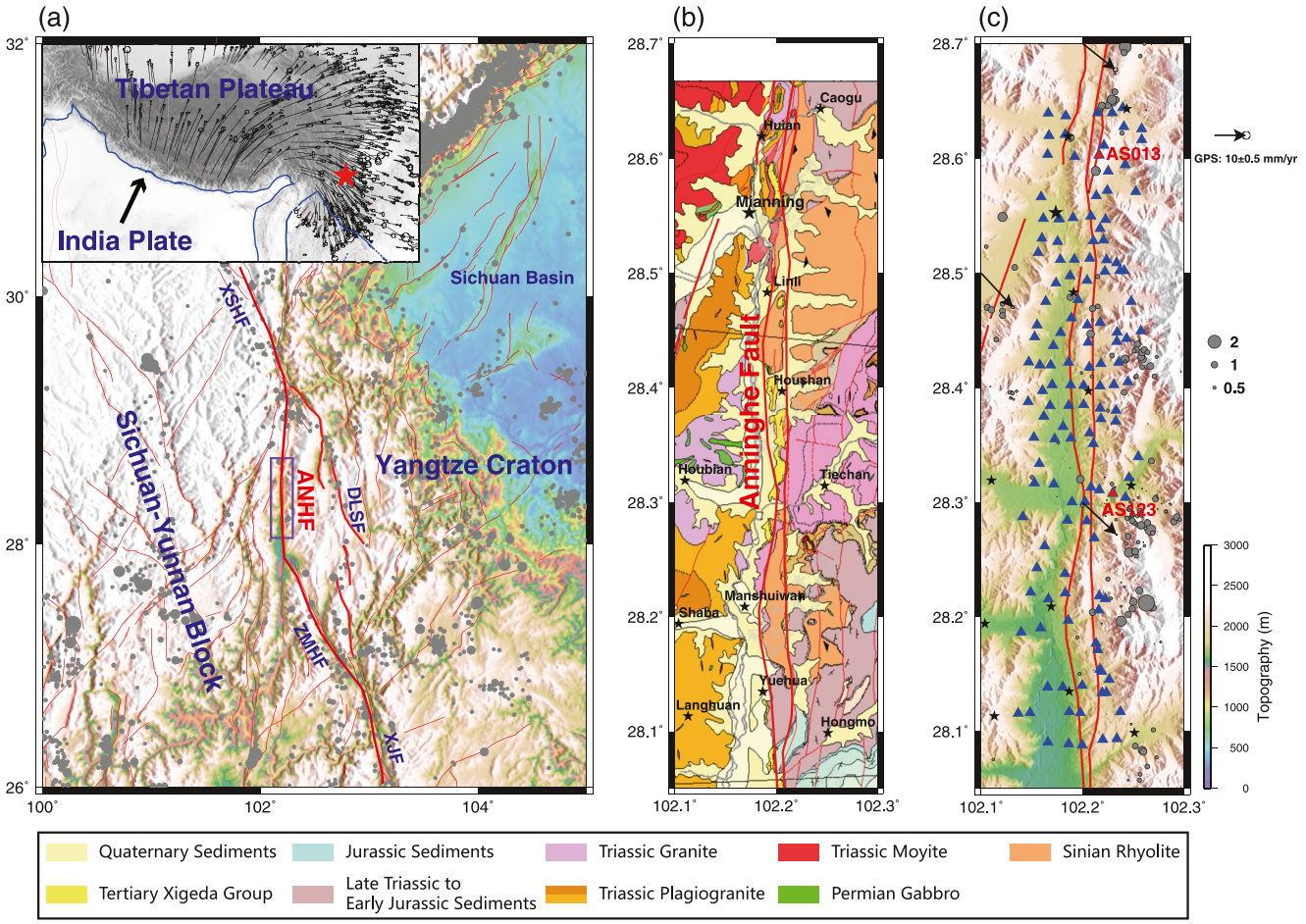

Figure 1. Tectonic, geological, and station distribution maps of the Anninghe fault zone and its surrounding areas. (a) The distributions of tectonic units, earthquakes, and global positioning system (GPS) data. The main tectonic units include the Yangtze Craton, the Sichuan-Yunnan Block, the Sichuan Basin, and the Xianshuihe fault (XSHF), Anninghe fault (ANHF), Daliangshan fault (DLSF), Zemuhe fault (ZMHF), and Xiaojiang fault (XJF). The earthquake data (gray dots) were collected from 1970 to 2012 with a magnitude greater than 3.0 (Z. Zhang et al., 2020). The purple rectangle identifies the study region. Two major tectonic units are shown in the top-left inset: the India plate and the Tibetan Plateau. The red star indicates the location of the study region. The short lines with arrowheads indicate GPS velocity vectors relative to stable Eurasia (Zhao et al., 2015). (b) Geological map of the study region (SGBMG, 1967). The lower panel displays the lithological legend. Middle thick red lines represent the Anninghe fault, which consists of the eastern and western branches. Black stars indicate the locations of the main city (Mianning) and villages (Caogu, Huian, Linli, Houshan, Houbian, Tiechan, Manshuiwan, Shaba, Yuehua, Langhuan, Hongmo) (c) Distributions of stations, microseismic events, and GPS data in the study region. The locations of the stations are indicated by blue triangles. The two red triangles (denoted by AS013 and AS123) indicate the example stations used in Figure 2. Gray dots with varying sizes represent microseismic events detected by the Xichang array between 13 January 2013 and 28 January 2019 with magnitudes ranging from M_L 0.5 to M_L 2.5 (Feng et al., 2021). The black arrows indicate the GPS velocity vectors (Zhao et al., 2015).

velocity structure beneath the Anninghe fault, which limits our understanding of its seismotectonics and the large earthquake hazards it potentially produces.

The ambient noise tomography (ANT) developed in recent decades has provided an effective approach for the study of the 3D fine structure of fault zones. A number of fault zones around the world have been investigated using ANT (e.g., Ben-Zion et al., 2019; Castellanos & Clayton, 2021; Gu et al., 2018; C. Li et al., 2020; H. Li et al., 2009; S. Luo et al., 2021; Mordret et al., 2019; H. F. Yang et al., 2020; H. F. Yang et al., 2021). We deployed a dense seismic array of short-period seismometers (Figure 1) to investigate the fine structure of the upper crust of the Anninghe fault zone. Nevertheless, previous studies have shown that the Sichuan-Yunnan region is highly affected by teleseismic body-wave noise sources in the period bands of 4–8 and 8–12 s (e.g., W. Wang, Gerstoft, & Wang, 2018). This usually produces near zero-time-lag body-wave noise in the ambient noise cross-correlation functions (CCFs) that will contaminate the desired surface waves for ANT. Thus, the quality of the anticipated tomography should be seriously compromised. To resolve this issue, we introduced a mode separation method based on the high-resolution linear Radon transform (HLRT) in exploration/engineering seismology to suppress the interfered noise from ambient noise CCFs.

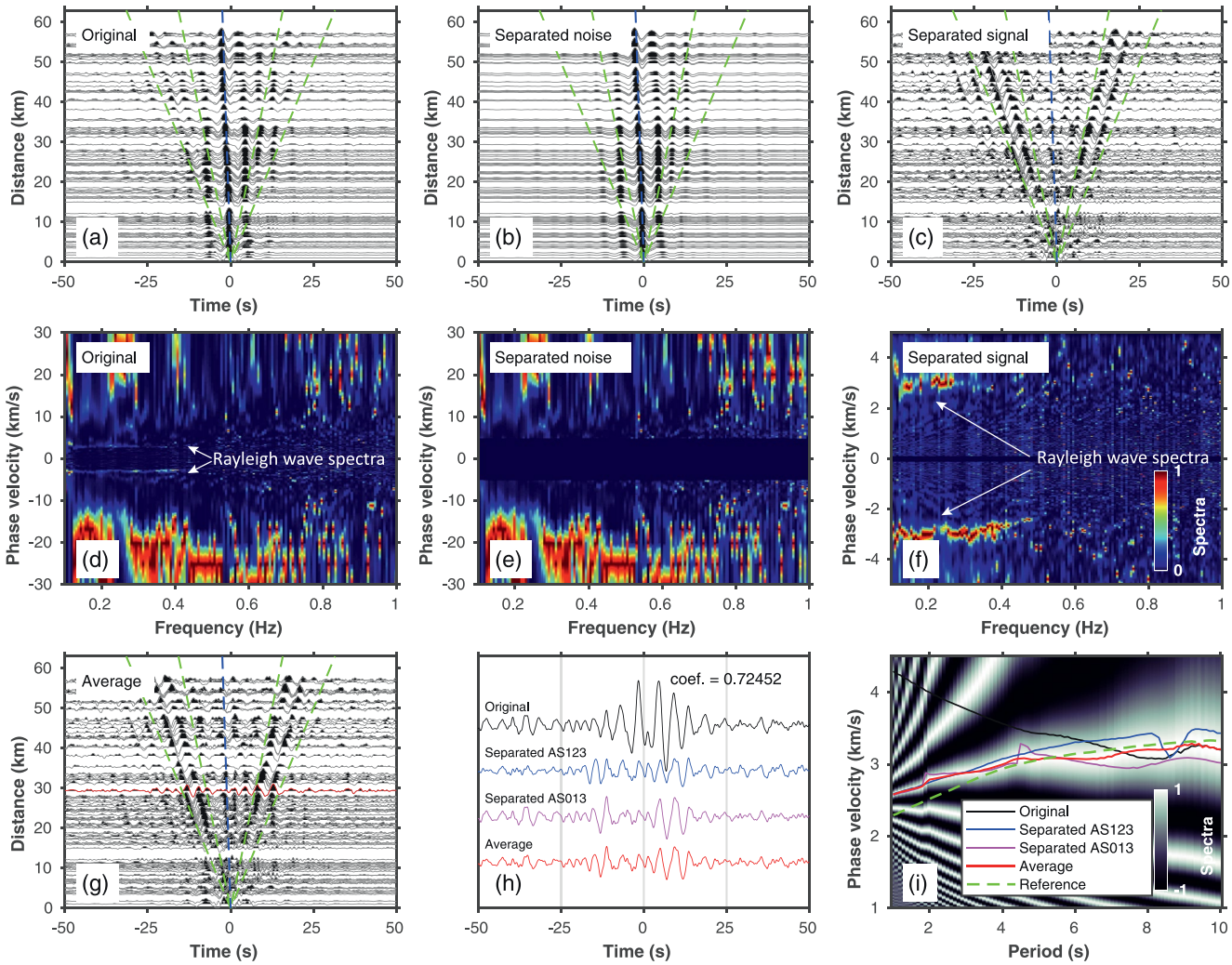

Figure 2. An illustration of the mode separation of Anninghe array cross-correlation functions (CCFs). (a–c) The CCF gathers of virtual source AS013 for the original, separated interfered noise, and target signals. All CCF gathers are filtered with a period band of 1–10 s. Green dashed lines indicate apparent velocities of 2 and 4 km/s. The blue dashed line represents the track of the interfered noise with an apparent velocity of 25 km/s. (d) Frequency-velocity spectra of the original CCF gather in (a). (e–f) The separated frequency-velocity spectra used to determine the separated interfered noise in (b) and target signals in (c), respectively. (g) The CCF gathers of virtual source AS013 for the average target signals. The red trace in (g) illustrates the selected example CCF (between stations AS013 and AS123) that is further explored in (h and i). (h) From top to bottom, the CCF waveforms for the original (black line), the separated target signals of virtual source AS123 (blue line), the separated target signals of virtual source AS013 (magenta line), and the average target signals (red line). The top right corner shows the correlation coefficient between the two separated target signals. (i) The dispersion spectra of the average target signals were calculated using the image analysis technique (H. Yao et al., 2006). The green dashed line represents the average dispersion curve from Figure 3b. The black, blue, magenta, and red lines represent the automatically picked dispersion curves from the dispersion spectra of the original, the separated target signals of virtual source AS123, the separated target signals of virtual source AS013, and the average target signals, respectively.

In this study, we first described the study region and data acquisition in the Anninghe fault zone. Following this, we provided a detailed explanation of how the HLRT suppresses interfered noise from ambient noise CCFs. We then used direct surface wave tomography (Fang et al., 2015) to obtain a 3D fine upper crustal structure beneath the Anninghe fault. Finally, we discussed the seismotectonic model and the importance of fine structures in the assessment of large earthquake hazards in the Anninghe fault zone based on the new fine velocity model.

2. Study Region and Data Acquisition

2.1. Study Region

The study region lies at the junction of the Sichuan-Yunnan block and the Yangtze Craton (Figure 1a). It includes a long and narrow portion in the central and southern parts of the Anninghe fault zone (latitude range: 28.05°–28.7°;

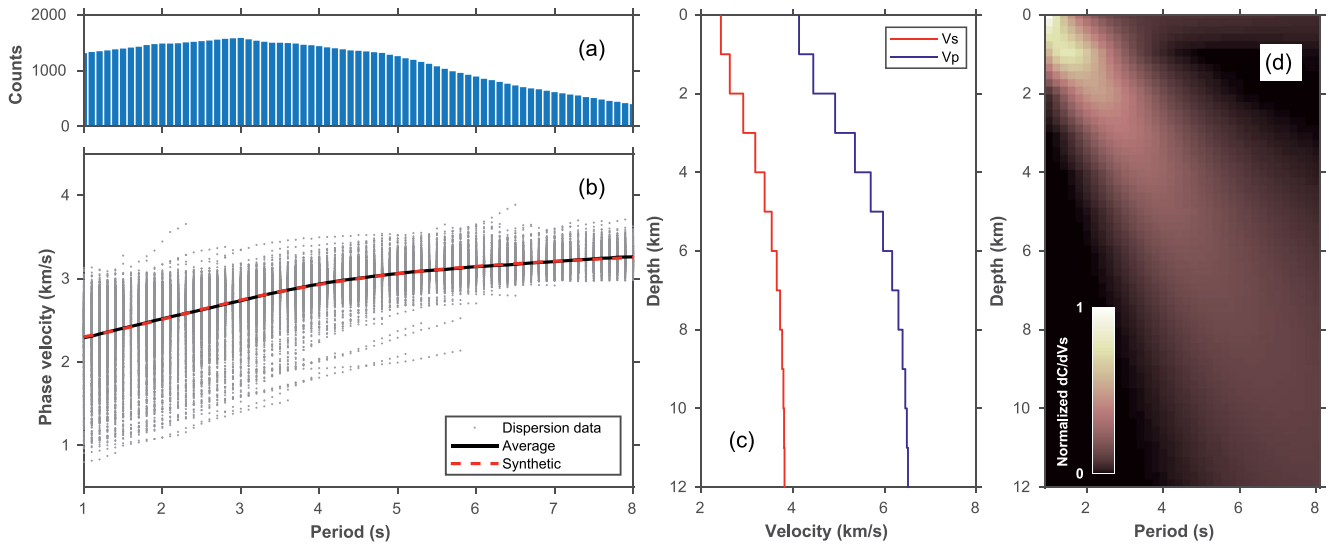

Figure 3. Results of Rayleigh wave dispersion analysis of the Anninghe array. (a) The number of dispersion data at different periods. (b) Dispersion data distribution (gray dots). The black line represents the average dispersion curve. The red dashed line indicates the synthetic dispersion curve generated using the 1D structural model in (c). (c) The inverted 1D *Vs* (red line) and *Vp* (blue line) structures from the average dispersion curve in (b). (c) Sensitivity kernel of dispersion data with respect to *Vs* at various depths and periods.

longitude range: 102.1°–102.3°; Figure 1). Within the study area, the Anninghe fault zone strikes approximately north-south. The Xianshuihe fault and the Zemuhe fault connect the northern and southern ends of the Anninghe fault, respectively (Figure 1a). In the east, there is the Daliangshan fault. A total of four major faults, namely, the Xianshuihe fault, the Anninghe fault, the Zemuhe fault, and the Xiaojiang fault, make up the eastern boundary of the Sichuan-Yunnan diamond block, which is the most seismically active region of the Sichuan-Yunnan region of China (Figure 1a). The study region contains strata ranging from Precambrian to Quaternary. Most of the Anninghe valley is situated on the west side of the Anninghe fault zone, containing the Tertiary Xigeda Group and Quaternary sediments (Figure 1b). The Anninghe fault zone crosses strata from the Precambrian and Mesozoic to the Cenozoic (Figure 1b; e.g., Y. Chen et al., 2021). One county-level city (Mianning) and several villages are included in the study area, which is mainly distributed along the Anninghe valley (Figure 1b).

2.2. Data Acquisition

As part of a research project to detect fine structures of fault zones, the University of Science and Technology of China, the Chinese University of Hong Kong, and the Institute of Geophysics of the China Earthquake Administration jointly deployed 134 three-component short-period seismometers (instrument type: QS-5A) with a natural period of 5 s and an average interstation spacing of ∼5 km along the southern central Anninghe fault in an area of 10×60 km^2 (Figure 1c). The Anninghe array was deployed from mid-October 2019 to early March 2020 with an average continuous recording time of approximately three months. Waveforms are sampled at a rate of 100 Hz.

3. Methodology

3.1. Calculation of Ambient Noise CCFs

First, the raw seismic data were reorganized by converting from SEED to SAC format, merging fragments, and downsampling them to 10 Hz, and daily files for each station were obtained. Using the daily vertical-component records, we calculated ambient noise CCFs (Bensen et al., 2007; Y. Zhang et al., 2018). For the calculation of CCFs, waveform data from a single station are preprocessed, including the removal of trend, mean, instrument response, time-domain normalization, and frequency domain whitening. To suppress the impact of dominant noise and earthquake periods, we applied a multiple-period normalization scheme (Y. Zhang et al., 2018), which tends to achieve a more even spectrum and enhance weak signals (Shen et al., 2012). Specifically, three-period bands (0.5–2, 2–5, and 5–10 s) are applied to the time-domain running-absolute-mean normalization. Finally,

the daily CCFs between all possible stations were stacked to enhance the signal-to-noise ratio. We inspected the daily and stacked CCFs as well as the teleseismic waveforms to eliminate stations with issues such as incorrect GPS time and weak signals. As a result of the inspection, 110 usable stations and 5,938 CCFs were determined.

Figure 2a illustrates the ambient noise CCFs between an example station (the red triangle, marked by AS013 in Figure 1c) and all other stations. Surface waves with apparent velocities between 2 and 4 km/s are detected in the CCFs. A distinctive feature of CCFs is the appearance of strong noise with an apparent velocity of approximately 25 km/s near zero time lag. This may be related to microseisms caused by teleseismic *P* waves coming from deep oceans (W. Wang, Gerstoft, & Wang, 2018). As a result, the near zero-lag-time noise can cause considerable interference with surface wave signals, especially for shorter interstation paths. It interferes directly with the extraction of the surface wave dispersion curve and can have detrimental effects on the subsequent tomography of the underlying structures. Here, we introduced a mode separation technique called the HLRT, which has been well developed in exploration/engineering seismology (e.g., Y. Luo et al., 2008, 2009; Trad et al., 2003), to eliminate near zero-lag-time signals from ambient noise CCFs.

3.2. Mode Separation of CCFs Using HLRT

A linear Radon transform (LRT) involves the transformation of a seismogram in the space-time domain to the Radon domain. Nevertheless, LRTs typically suffer from problems such as loss of resolution and aliasing (Trad et al., 2003). The HRLT addresses these issues by assuming a smooth amplitude variation in the transition between known and unknown data (Trad et al., 2003). It involves the transformation of seismograms in the space-time domain to the Radon domain by finding the best model with the fewest parameters to fit the data under a sparsity constraint (e.g., Y. Luo et al., 2009). In its original form, the HLRT was used to analyze seismograms from active sources (e.g., Y. Luo et al., 2008, 2009; Trad et al., 2003). Because CCFs are associated with empirical Green's functions (e.g., Lin et al., 2008; H. Yao et al., 2006), we can directly replace the seismograms of active sources with the CCFs of virtual sources. Consequently, the general procedure for separating modes in CCFs is similar to that for separating modes in seismograms (Y. Luo et al., 2009), although there are some differences since CCFs consist of both positive and negative time lags.

The following five steps are designed to automatically separate the near zero-lag-time noise and surface wave signals of the CCFs of the study region using HLRT. First, each station is selected as a virtual source, and the CCFs of each virtual source are extracted to form a virtual source gather in the space-time domain. Figure 2a shows an example of a CCF gather from virtual source AS013. Second, we performed HLRT on each virtual source gather of CCFs. The HLRT transforms the virtual source gather into the Radon domain (the frequency and slowness domain). The slowness spacing should be selected according to the rule proposed by Turner (1990) to avoid aliasing in the transformation. Here, the slowness spacing is set to 0.01 s/km. Considering that the CCFs contain both positive and negative time lags, we searched the slowness in positive and negative values, respectively, to account for forward and backward propagation waves. In practice, the slowness is replaced by velocity through interpolation, which results in frequency-velocity spectra that facilitate the selection of modes. The third step is to define a window for the target signals (surface waves). Because there are obvious differences in apparent velocity between the target signals and the interfered noise in the CCFs of the Anninghe array (Figure 2a), we set the velocity range to be 0.1–5 km/s and (−5)–(−0.1) km/s in the frequency-velocity spectrum so that target signals and interfered noise are divided accordingly (Figures 2d–2f). The fourth step involves transforming the target signals and interfered noise in the frequency-velocity/slowness domain back to the space-time domain. Figures 2b and 2c show the separated CCFs of the interfered noise and target signals following mode separation. The near zero-time-lag noise is clearly separated from the original CCFs, and the separated surface wave signals have improved greatly. Fifth, the above four steps have been completed for all virtual sources (or stations), and there will be two CCFs for each station pair, which should ideally be equivalent but can rarely be achieved in real situations due to heterogeneous structures and nonuniform wavefields. It is appropriate to take the average of these two target CCFs if their correlation coefficient is high (greater than 0.5) to be used in further processing of the data. Figure 2g shows the CCF gather after the averaging operation. Figure 2h shows the waveforms of CCFs for an example station pair, where the blue and magenta lines denote the two separated CCFs for virtual sources AS123 and AS013, respectively. The red line represents the average CCF. Figure 2i shows the dispersion analysis of the original, the two separated, and the average CCFs using an image analysis technique (H. Yao et al., 2006). The autopicked dispersion curves (red line in Figure 2i) after separation are improved significantly compared to the original ones (black line in Figure 2i).

We further demonstrated the effectiveness of this mode separation method using synthetic data in Appendix A, Text S1 and Figure S1 in Supporting Information S1 (e.g., Herrmann, 2013; Tromp et al., 2008).

3.3. Measurement of Surface Wave Dispersion Data

Based on the improved CCFs, we semimanually picked the Rayleigh wave phase velocity dispersion data using the image analysis technique (H. Yao et al., 2011, 2006). Figure 2i shows the dispersion image for one example CCF after mode separation. As a comparison, the dispersion curve extracted from CCFs before mode separation deviates significantly from the reference dispersion curve (Figure 2i). Furthermore, we performed a path cluster analysis (Y. Zhang et al., 2018) on the dispersion data to ensure data quality. Cluster analysis is based on the hypothesis that station pairs with similar ray paths should have similar dispersion curves (Y. Zhang et al., 2018). We eliminated dispersion data that deviated three (or more) times the standard deviation of the clustered dispersion data. As a result of the cluster analysis, 1983 dispersion curves with high quality (Figure 3b) are retained for subsequent tomography. There are approximately 500–1,500 measurements in the period band of 1–8 s (Figure 3a). Figure 3c shows the one-dimensional (1D) structural model obtained by inverting the average dispersion data (black line in Figure 3b). Based on the sensitivity analysis of this 1D structural model, it appears that the dispersion data in the period band of 1–8 s have a high sensitivity between 0 and 12 km in depth.

3.4. Direct Tomography of the 3D *Vs* Structure

By using the direct surface wave tomography method (Fang et al., 2015; C. Liu et al., 2019), we inverted all the mixed-path Rayleigh wave dispersion data for the 3D *Vs* structure. The direct tomography method takes into account curved ray paths due to 3D heterogeneous structures based on the fast marching method (Rawlinson & Sambridge, 2005) and partial sensitivity kernels of *Vp* and density based on empirical relationships (Brocher, 2005), which makes it an efficient tool for surface wave tomography. During tomography, the initial model is set as the 1D structural model in Figure 3c. *Vp* and density are derived from *Vs* based on their empirical relations (Brocher, 2005). Sensitivity analysis (Figure 3d) indicates that the depth range of sensitivity becomes wider for longer periods. Based on this, the depth grids have been empirically set to 0, 1, 2, 3, 4.5, 6, 8, 10, 12, 14, and 16 km, which have a small spacing at shallow depths but a large spacing at deep depths. The horizontal grid spacing is set at $0.01° \times 0.01°$. The weight factor between the travel time residual and model normalization is set to 10 upon the performance of the checkerboard tests (Figure 4).

4. Results

4.1. Checkerboard Tests

The checkerboard test is a standard procedure for a tomographic study to determine the resolution and recoverability of the 3D velocity model. We conducted checkerboard tests for two *Vs* models with different anomaly sizes. Specifically, the two *Vs* models have anomaly sizes of $0.04° \times 0.04°$ and $0.06° \times 0.06°$ horizontally and 0–3 and 4.5–16 km vertically (Figure 4). The amplitude of the *Vs* anomaly is ±8% of the 1D structural model in Figure 3c. Synthetic travel times are calculated using the two *Vs* models. To mimic real-world noise, 1% Gaussian noise is also added to the synthetic travel times. When tomography is performed, the synthetic data are treated as "observed" data. Checkerboard tests indicate that the dispersion data can constrain $0.04° \times 0.04°$ anomalies at shallow depths (~0–4 km) and $0.06° \times 0.06°$ anomalies at deeper depths (0–12 km). Nevertheless, checkerboard analysis should only be considered as a reference and not as an indicator of true recoverability since multiple other factors also influence the resolution of the model (Rawlinson & Spakman, 2016).

Additionally, we note that there is a topography variation between 1.5 and 2.5 km in the study region, which might affect the velocity model. Jin et al. (2023) reported a bias of up to −4% at a depth of 5 km, in the presence of significant topographic variation (~4 km). Based on the empirical relations between elevation difference and tomographic bias ($y = -1.04x - 0.5$, where x is elevation difference, y is topographic bias; Jin et al., 2023), the tomographic bias is approximately −1.5% (~0.045 km/s) in this study region with an elevation difference of about 1 km, which should have only a slight effect on the velocity variations we are focusing on (>0.2 km/s, Figure 5).

4.2. 3D *Vs* Structure Beneath the Anninghe Fault

Figure 5 shows horizontal slices of *Vs* at depths of 1, 3, 4.5, and 8 km beneath the southern central Anninghe fault zone. One distinctive feature of the *Vs* structure is the presence of a narrow low-velocity belt spreading in the N-S

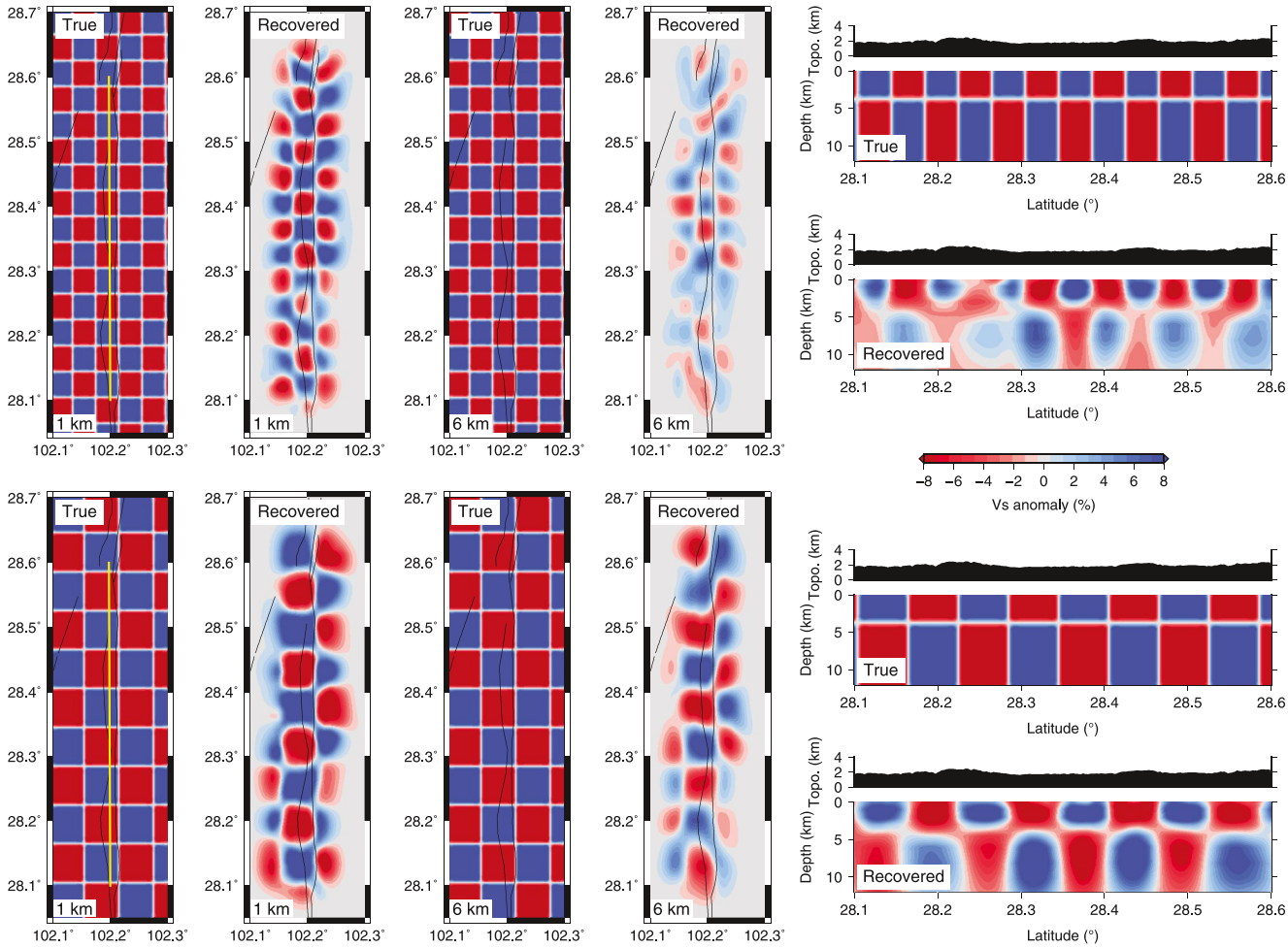

Figure 4. Results of checkerboard tests. The top six panels illustrate the results of the checkerboard model with an anomaly size of 0.04° × 0.04°. The lower six panels are for the checkerboard model with an anomaly size of 0.06° × 0.06°. In the left 1 km slices, yellow lines indicate the horizontal locations of the vertical profiles on the right side.

direction at shallow depths of 1–3 km. The narrow low-velocity belt has a width of approximately 4–5 km and is closely related to the Anninghe fault zone. In contrast, the western and eastern mountain areas exhibit a general high-velocity feature at shallow depths (Figures 5a and 5b).

At depths of 4.5 and 8 km, the narrow low-velocity belt shifts to the east for a distance of ~5 km (Figure 5d). Based on the checkerboard analysis (Figure 4) and recovery test (Text S2 and Figure S2 in Supporting Information S1), the east-shifted low-velocity belt can be resolvable. Additionally, it correlates with the location of seismicity detected by the Xichang array (Feng et al., 2021).

In Figure 6, vertical *Vs* profiles are shown across the Anninghe fault zone. Further evidence is provided by these profiles that low-velocity structures underlie the Anninghe fault zone at shallow depths and shift eastward as depth increases. There is also a consistent relationship between the east-shifted low-velocity belt and local seismicity, especially at profiles of lat. = 28.25°, lat. = 28.3°, and lat. = 28.35° (Figures 6c–6e).

5. Discussion

As one of the components of the Xianshuihe-Xiaojiang fault system, the Anninghe fault plays a significant role in accommodating crustal material extrusion around the eastern Himalayan syntaxis in the SE Tibetan Plateau (e.g., Schoenbohm et al., 2006; Q. Wang et al., 2001). Moreover, the Anninghe fault is recognized as a present-day seismic gap zone that has the potential for a large earthquake with a magnitude greater than 7 (e.g., Wen et al., 2008).

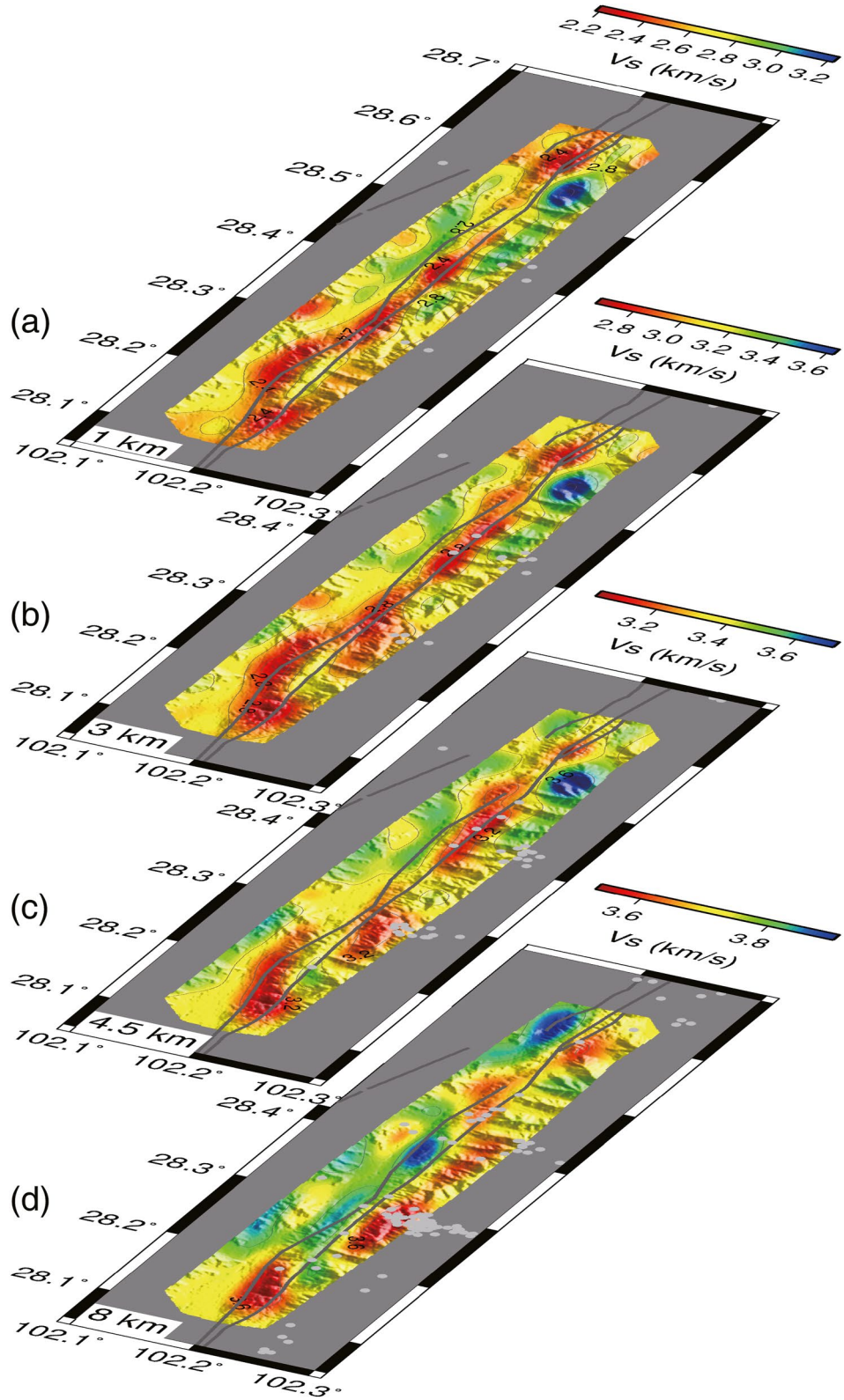

Figure 5. (a–d) Horizontal slices of *Vs* at depths of 1, 3, 4.5, and 8 km. The gray dots represent the locations of microseismic events detected from the Xichang array by Feng et al. (2021).

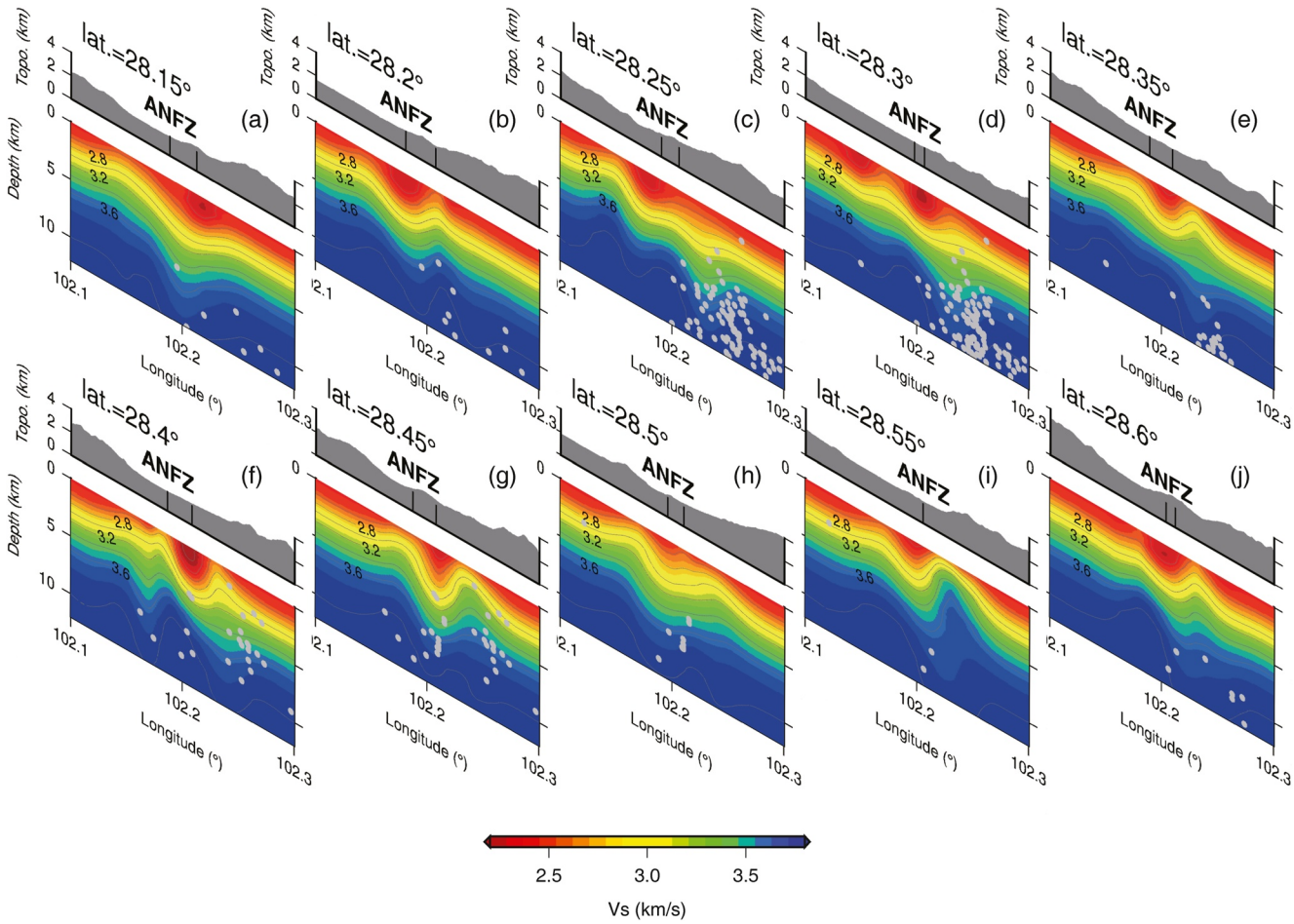

Figure 6. (a–i) Vertical profiles of *Vs* along fixed latitudes of 28.15°, 28.2°, 28.25°, 28.3°, 28.35°, 28.4°, 28.45°, 28.5°, 28.55°, and 28.6°, respectively. The gray dots represent the locations of microseismic events detected from the Xichang array by Feng et al. (2021).

With the help of a newly deployed dense array, this study proposes the HLRT mode-separation method to suppress near zero-time-lag interfered noise in ambient noise CCFs and constructs a 3D upper crustal *Vs* model beneath the southern central Anninghe fault zone. This fine 3D *Vs* model sheds new light on the geometry of the fault plane, local seismotectonics, and potential large earthquake hazards of the Anninghe fault zone in the future.

5.1. Formation of the Narrow Low-Velocity Belt

One distinctive feature of the fine structure is the narrow low-velocity belt along the Anninghe fault zone (Figure 5). The narrow belt of low velocity gradually shifts eastward at deeper depths. The shift is consistent with the distribution of local microseismic events at deep depths, which indicates a close tectonic relationship between them (Figure 6). Despite the lack of reports on the 3D upper crustal structure beneath the Anninghe fault, several previous studies have obtained 2D profiles of electrical and velocity structures across the Anninghe fault (e.g., Shao et al., 2022; Wan et al., 2010; Z. Yang et al., 2011).

Using magnetotelluric sounding, Wan et al. (2010) determined a 2D electrical profile along the Mianning-Yibin (in the northern margin of this study region). According to their results, the Anninghe fault zone is a highly conductivity zone with a width of ~5 km, extending to the middle crust (greater than 20 km), in sharp contrast to the high resistance on both sides. Both the width and shape of the low-velocity belt detected in this study are in agreement with the 5 km wide vertically low-resistance zone discovered by Wan et al. (2010). Z. Yang et al. (2011) obtained a 2D *Vp* profile at the southern end of the Anninghe fault (near Xichang city) using the

first arrival of refracted waves from active sources. They found that the upper crust of the Anninghe fault exhibits a low-velocity zone extending from the surface to depths of approximately 6–7 km and dipping northeastward. Despite the fact that the location of the 2D profile of Z. Yang et al. (2011) is outside the scope of this study, it also represents the typical characteristics of the southern end of the Anninghe fault zone and is consistent with our findings of the low-velocity belt. Recently, Shao et al. (2022) obtained three *Vp* profiles across the Anninghe fault based on direct *P* wave travel time data from methane gas sources. They found prominent low-velocity anomalies beneath the Anninghe fault zone in the shallow 2 km, which is also consistent with the low-velocity belt in this study.

The consistency between the low-velocity belt revealed in this study and the previously discovered high-conductivity zone and low *Vp* zone suggests that they are the result of the same physical structure. It has been suggested that crustal high-conductivity zones are generally associated with areas of high seismic activity (Wan et al., 2010). Meanwhile, Z. Yang et al. (2011) concluded that the low *Vp* zone extending to 6–7 km was the result of fractured basements due to compression. In contrast, Shao et al. (2022) believed that the low velocity beneath the Anninghe fault may be associated with Quaternary sediments based on the local geological map. A limitation of these studies is the reliance on 2D profiles, which limits their ability to interpret the results. This study reveals a narrow low-velocity belt that runs through areas of multiple rock types, including Quaternary sediment, Tertiary Xigeda Group, and Sinian rhyolite (Figure 1c), indicating that rock phases are not the primary factor contributing to the low-velocity belt at greater depths. Taking into account the highly conductive features, it is reasonable to speculate that the narrow low-velocity belt is a fracture zone that contains water due to transpression and sinistral strike-slip movements along the Anninghe fault. A shallow surface drilling study partially supports this hypothesis. For example, G. Hu et al. (2016) analyzed the data from two 100 m deep boreholes in the Mianning-Xichang segment, showing that the formations are fragmented over the entire depth range.

5.2. Seismotectonic Model of the Anninghe Fault

Through strike-slip and thrust movement, the Anninghe fault reconciles the clockwise rotation of crustal material around the eastern Himalayan syntaxis due to the subduction of the Indian plate underneath the Eurasian plate. The strike-slip movement dominates the N-S direction of material migration, while the E-W thrust movement absorbs the compression and shortening in the E-W direction, resulting in the uplift of the ridge between the eastern and western branches of the Anninghe fault (e.g., Ren, 2014). Nevertheless, there is still controversy over the exact tectonic model of the Anninghe fault.

Based on their focal mechanism solution, G. Chen et al. (2008) deduced that the eastern and western branches of the Anninghe fault become one uniformly oblique-slip fault at deep depths; moreover, their interpretations indicate that the western branch of the Anninghe fault is a nearly vertical plane and acts primarily as a strike-slip component, whereas the eastern branch dips west and primarily acts as a thrust component. It is evident that this west-dipping deduction of the fault plane does not correspond to the east-dipping low-velocity zone revealed in this study and to the NE-dipping low *Vp* zone revealed in Z. Yang et al. (2011). Additionally, regional imaging results indicate that the western areas of the Anninghe fault zone exhibit high-velocity anomalies, while the eastern areas exhibit low-velocity anomalies (e.g., W. Liu et al., 2019; Z. Zhang et al., 2020). Therefore, it can be concluded that the western areas of the Anninghe fault are generally more rigid than the eastern areas, resulting in the western side being inserted below the eastern side under the WNW-ESE compressional regime. While there is only a small vertical slip rate difference between the eastern and western areas today (e.g., Su et al., 2017), G. Chen et al. (2008) derived that there are at least 1 mm/a slip rate differences based on topographic sections across the Anninghe fault, where the western area is depressed and the eastern area is relatively uplifted.

Based on previous results and new findings from the fine *Vs* model of this study, we propose a seismotectonic model of the Anninghe fault (Figure 7). As a component of the Xianshuihe-Xiaojiang fault system, the Anninghe fault zone accommodates the rotation of crustal material around the eastern Himalayan syntaxis through strike-slip and thrust activities (e.g., Ren, 2014). Although previous studies have suggested that the Anninghe fault may eventually be replaced by the Daliangshan fault to the east as a result of shortcutting (He et al., 2008), the current Anninghe fault still has a large strike-slip component, making it a zone with a high risk of a large earthquake of magnitude greater than 7 in the future (Wen et al., 2008; S. Yao & Yang, 2022). As a result of the strike-slip and thrust movement between the two branches (i.e., the eastern and western branches of the Anninghe fault), the narrow zone between the two branches has gradually fractured and uplifted, creating the present-day topography

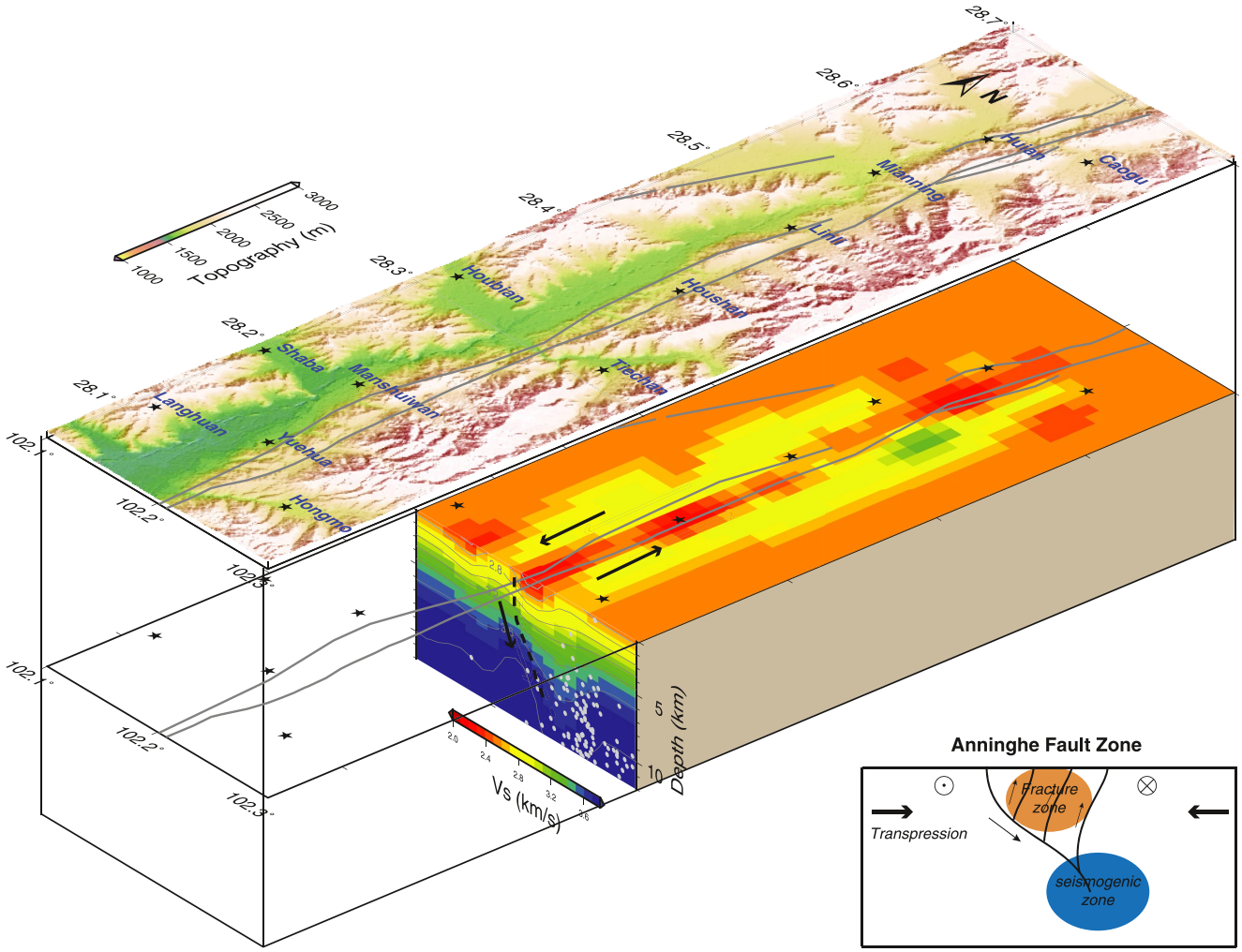

Figure 7. An interpretation of the seismotectonic model beneath the Anninghe fault. In the vertical *Vs* profile, the arrow indicates the direction of the interpreted thrust fault. The arrows in the horizontal slice indicate the current sinistral strike-slip movement of the Anninghe fault. The gray dots represent the locations of microseismic events detected from the Xichang array by Feng et al. (2021). A schematic diagram of the interpretation is shown in the lower right panel. Please refer to the context for more interpretation.

of "two grabens and one base" (Y. Chen et al., 2021; Ren, 2014). In addition, the transpression resulted in the rigid western areas being inserted underneath the weaker eastern areas, resulting in an east-dipping fault plane. At depths greater than 5 km, the addition of water may weaken the mechanical strength of deep rocks, leading to a seismogenic zone with enhanced microseismic activity.

5.3. Simulation of Large Earthquake Hazards Based on the Final *Vs* Model

Many previous studies have shown that the Anninghe fault is a seismic gap and has a high risk of a destructive earthquake of magnitude greater than 7 (e.g., Cheng et al., 2010; Y. C. Li, Nocquet, Shan, & Jian, 2021; Wen et al., 2008; S. Yao & Yang, 2022; Yi et al., 2008). By simulating scenario earthquake ruptures using the fine upper crustal structure obtained in this study, we are able to conduct the investigation more reliably.

The first regional community velocity model in the Sichuan-Yunnan area, SWChinaCVM-1.0 (Y. Liu et al., 2021; H. Yao, 2020), is referred to as Model 1 and is used as a reference structural model. Since the fine model obtained in this study is at the upper crust scale, we constructed Model 2 by combining the fine upper crustal model with the SWChinaCVM-1.0 model. According to the research of S. Yao and Yang (2022), it is unlikely that the potential earthquake will rupture through the entire Anninghe fault; instead, it may rupture across three high-stress zones from Shimian to Xichang, resulting in earthquakes with magnitudes of

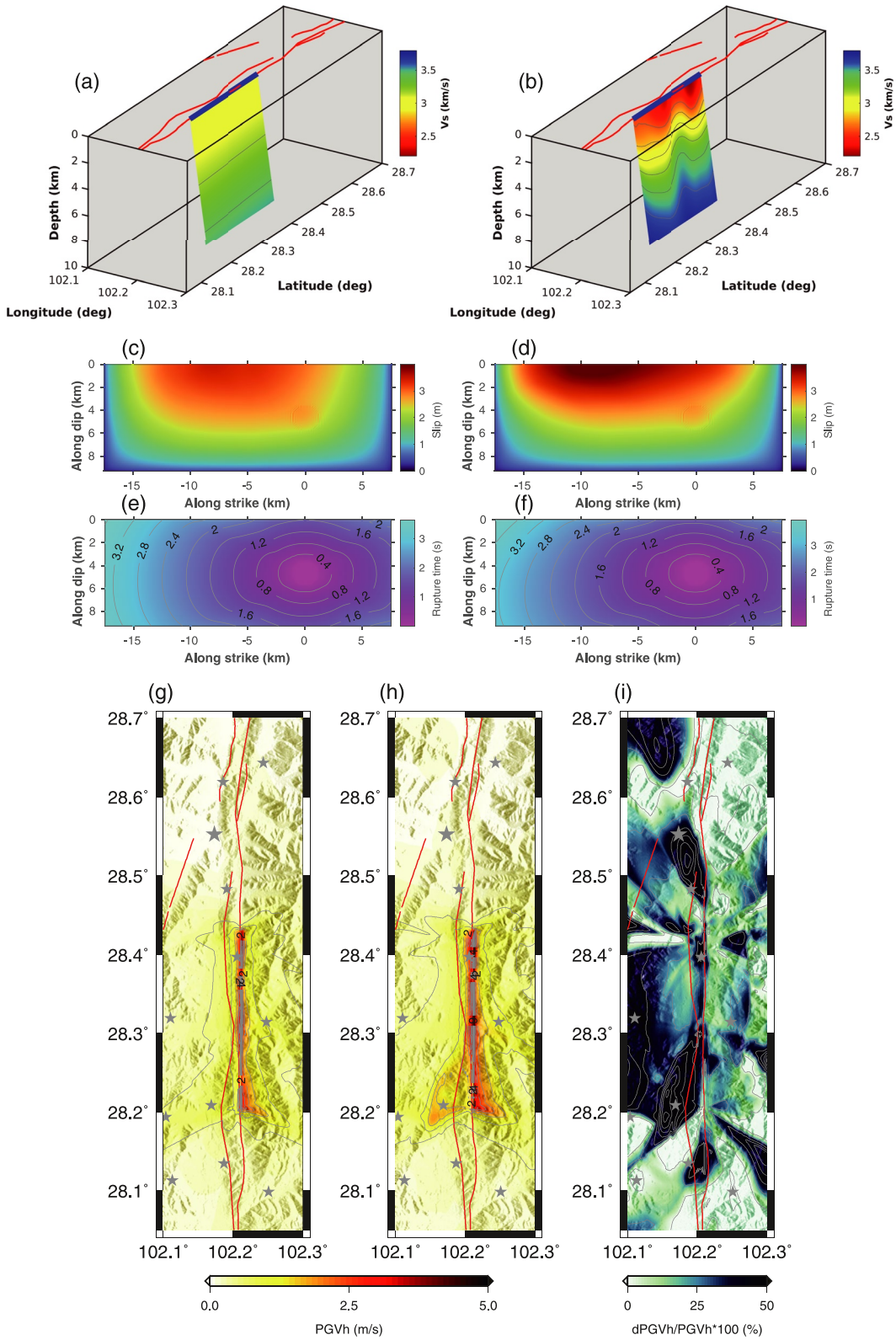

Figure 8.

approximately 7. In our study region, there is exactly the central high-stress zone located south of Mianning city; meanwhile, it is also a location with many microseismic events (Figure 1c), which might indicate the possibility of a future large earthquake. Therefore, we set up a 25 km long and 10 km wide rupture plane along the more active eastern branch of the Anninghe fault (Figures 8a and 8b) to simulate a scenario of a strong earthquake with a magnitude of approximately 7. In addition, according to the fine structure obtained in this study, the dip angle is approximately 68° eastward, which is used in the rupture simulation. Figures 8a and 8b illustrate the 3D view of the fault plane and the variations in shear wave velocity on it. Compared to the reference model (Figure 8a), the fine structure obtained in this study provides a greater level of detailed velocity variations on the fault plane (Figure 8b). The nucleation zone is defined as a circle with a radius of 1.2 km located at the epicenter with a depth of 5 km. To initiate the rupture process, the shear stress in the nucleation zone is set to be slightly higher (0.5%) than in other areas of the plane. A curved grid finite difference method (CG-FDM; W. Zhang & Chen, 2006; Z. Zhang et al., 2014) was employed to simulate the dynamic rupture process of the fault and the propagation of seismic waves for Model 1 and Model 2, respectively. During the simulation, the initial stress distribution is assumed to be uniform, and the influence of topographic relief is not taken into account.

As a result of the difference in velocity structure, Model 1 and Model 2 produce earthquake magnitudes of Mw = 6.72 and Mw = 6.71, respectively. Figures 8c and 8d show the slip distribution on the fault plane. The peak slips of both models are located near the surface, whereas the slips of Model 2 are clearly intensified in comparison with those of Model 1. The distribution of rupture time is shown in Figures 8e and 8f. Near the surface, Model 2 has slower rupture speeds than Model 1 as a result of its lower velocities. Figures 8g–8i illustrate the distribution of the horizontal peak ground velocity (PGVh) calculated by Model 1 and Model 2, as well as the difference between the two distributions. Due to the eastward dip of the fault plane, the PGVh distributions are not symmetrical with respect to the rupture zone, and the higher PGVh lies slightly to the east. Compared to Model 1, the PGVh of Model 2 shows a wider intensity range than the PGVh of Model 1, particularly near 28.2° on the western side of the fault, where the intensity is significantly increased and is consistent with low-velocity anomalies. Figure 8i illustrates the difference in distribution between the two (calculated by (PGVh2 − PGVh1)/PGVh1 × 100%). In most areas, PGVh intensities increase by ∼25%–50% when the fine structure is considered, particularly along the narrow low-velocity belts. This should be related to the enhancement of the strong ground motions induced by low-velocity anomalies (e.g., Wirth et al., 2019). In addition, we found that Mianning city is located in an area with significant PGVh enhancement (Figure 8i), which further illustrates, from another perspective, that the fine structure plays an important role in the prediction of large earthquake hazards in the Anninghe fault zone.

6. Conclusion

In this study, we obtained a fine 3D upper crustal *Vs* model beneath the southern central Anninghe fault zone using a newly deployed dense array. We proposed using the HLRT mode-separation technique to suppress zero-lag-time interfered noise from ambient noise CCFs. With mode separation, the surface wave signals are greatly enhanced, which is critical for obtaining high-quality tomography. The obtained fine structures reveal a narrow low-velocity belt along the Anninghe fault within a depth of 3 km. The narrow low-velocity belt shifts to the eastern areas at depths of 4.5–8 km. In light of previous insights and new findings of the fine structures in the Anninghe fault, we propose a seismotectonic model that interprets the narrow low-velocity belt as a water-contained fractured zone; meanwhile, a seismogenic zone is found beneath the eastern areas of the Anninghe fault at deeper depths as a result of the transpressive tectonic regime. When the 3D fine structure was used for scenario earthquake simulations, the PGAh increased by approximately ∼25%–50% compared with the smooth regional model in the rupture simulation, which highlights the significance of fine velocity structures in assessing large earthquake hazards.

Figure 8. Results of a scenario earthquake simulation in the Anninghe fault using two different *Vs* models. (a–b) 3D view of rupture planes and variations in *Vs*, where *Vs* in (a) comes from SWChinaCVM-1.0 (Model 1; Y. Liu et al., 2021), while *Vs* in (b) comes from this study's fine structure (Model 2). (c–d) Distributions of slips on the fault plane using Model 1 and Model 2, respectively. (e–f) Distributions of rupture time on the fault plane based on Model 1 and Model 2, respectively. (g–h) Distributions of horizontal peak ground velocity (PGVh) using Model 1 and Model 2, respectively. (e) The percentage difference in PGVh between Model 1 and Model 2.

Appendix A: Mode Separation of CCFs Using HLRT to Synthetic Data

The mode separation method is applied to synthetic data to further validate its effectiveness. Using the modal summation method (10 modes) in the Computer Programs in Seismology package (Herrmann, 2013), we simulated 36,000 s three-component (Z, N, and E) continuous waveform data that contain the fundamental and overtones of both Rayleigh and Love waves (Figure A1c). The simulation involves 10,000 noise sources placed in a ring-shaped area (with a minimum radius r_{min} = 100 km and maximum radius r_{max} = 150 km) surrounding the Anninghe array (Figures A1a–A1b). The 1D structural model in Figure 3c is used as an input model. After simu-

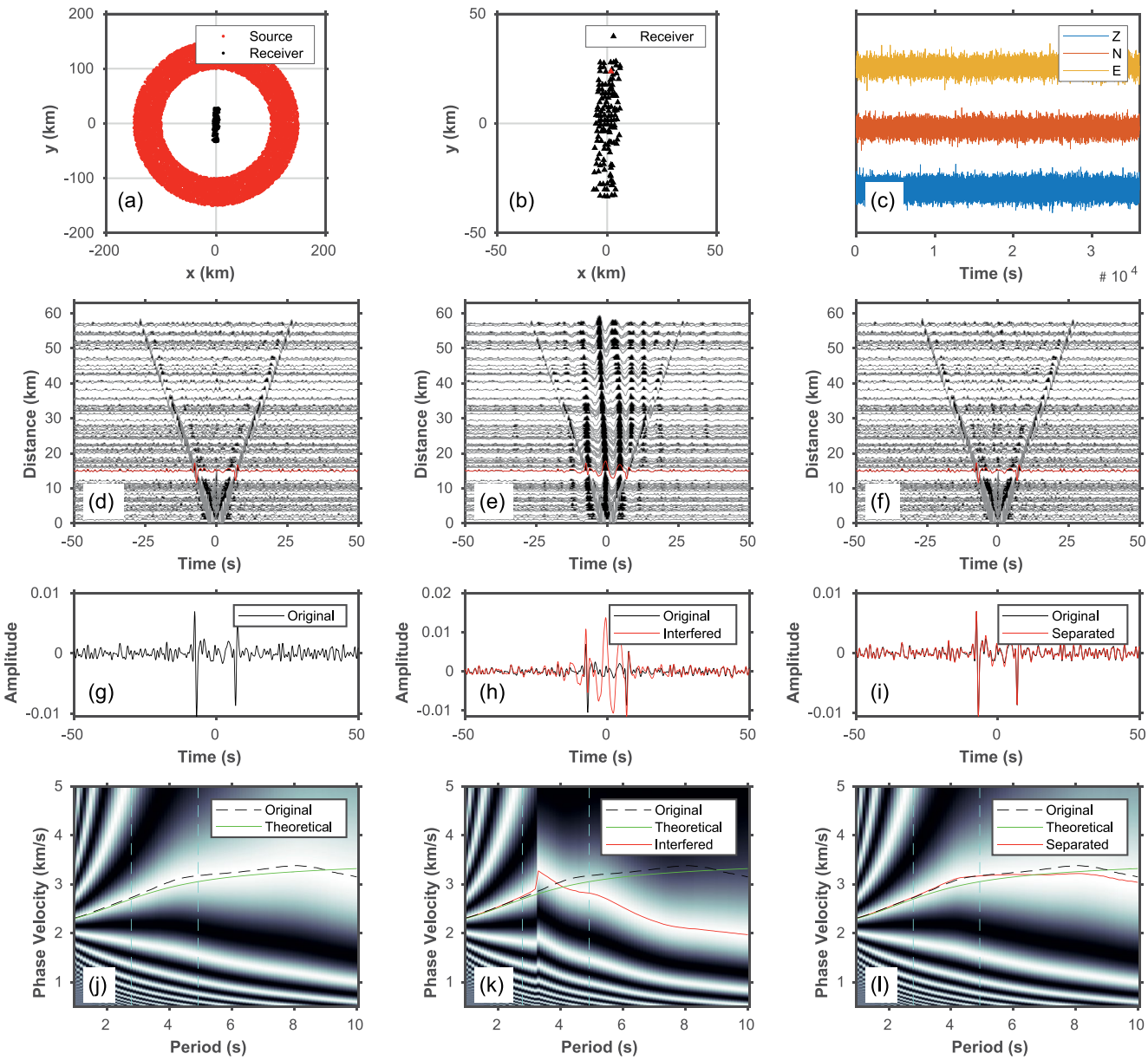

Figure A1. Results of mode separation of cross-correlation functions (CCFs) using synthetic ambient noise data. (a) The configuration of 10,000 noise sources (red dots) and 110 receivers (black dots). (b) The enlarged map shows the detailed distribution of receivers in (a). The red triangle represents the example receiver that is used to display the three-component records in (c). (c) The simulated three-component records of an example receiver in (b). (d–f) The original, near zero-time-lag interfered, and separated virtual source gathers of CCFs of the example receiver, respectively. Red lines in (d–f) indicate the selected CCFs in (g–i), respectively. (g–i) Comparison of the original, interfered, and separated CCFs. (j–l) Surface wave dispersion spectra determined from the original, interfered, and separated CCFs. Green lines represent theoretical dispersion data. The black dashed lines represent the autopicked dispersion curves based on the peak energy of the original dispersion spectra. The red lines in (k–l) represent the autopicked dispersion curves derived from the dispersion spectra of interfered and separated CCFs. Vertical cyan lines indicate periods in which the wavelength is equal to one or two times the interstation distance.

lation, we added random noise with a magnitude of one standard deviation of the synthetic data to the synthetic data to mimic real-world noise. Using the Z-component records, we calculated the CCFs for all station pairs. A virtual source gather of CCFs is shown in Figure A1d, in which Rayleigh wave signals are observed in both positive and negative time lags.

To simulate near zero-time-lag interfered noise in CCFs, we transformed the synthetic space-time CCFs into the Radon domain, added interfered energy from field data, and then transformed them back into the space-time domain. Figure A1e shows the near zero-time-lag interfered CCFs as a result of these operations. The mode separation using HLRT was then applied to the CCFs with near zero-time-lag interfered noise. As a result of the separation process, we obtained clean CCFs (Figure A1f) that are nearly identical to the original CCFs (Figure A1d), which validates the effectiveness of the separation. Waveform comparisons of the CCFs of an example receiver pair are shown in Figures A1g–A1i. Based on the image analysis technique (H. Yao et al., 2006), we calculated their dispersion spectra (Figures A1j–A1l). The near zero-time-lag noise distorts the dispersion spectra, especially at long periods (Figure A1k). The distorted dispersion spectra are repaired significantly after mode separation (Figure A1l).

Data Availability Statement

The portable station data are archived at the China Seismic Array Data Management Center at the Institute of Geophysics, China Earthquake Administration (https://doi.org/10.12001/ChinArray.Data, http://www.chinarraydmc.cn). The primary and processed data containing the CCFs of ambient noise, dispersion data, and the final 3D *Vs* model beneath the Anninghe fault in this research can be accessed at https://doi.org/10.5281/zenodo.7513262.

Acknowledgments
The authors thank two anonymous reviewers and the Editor Professor Michael Bostock for their constructive comments. The authors appreciate the help and useful discussion from Shaoqian Hu (CUG), Jikun Feng (USTC), Xihui Shao (USTC), and Ying Liu (USTC) in the data analysis. The authors would also like to thank Prof. Robert Herrmann for sharing the Computer Programs in Seismology package and the scripts for simulating ambient noise (https://www.eas.slu.edu/eqc/eqc_cps/TUTORIAL/HFAMBIENTNOISE/hfambient-noise.html, last accessed 8 January 2023). Figures were generated using Generic Mapping Tools (GMT; Wessel et al., 2013) and MATLAB software. This study was jointly supported by the Key Research and Development Program of China (2021YFC3000704, 2018YFC1503400), the National Natural Science Foundation of China (42004031, 42125401), the special fund of Key Laboratory of Earthquake Prediction, CEA (2021IEF0103), and the Anhui Key Research and Development Program of China (202104a07020016).

References

Bensen, G. D., Ritzwoller, M. H., Barmin, M. P., Levshin, A. L., Lin, F., Moschetti, M. P., et al. (2007). Processing seismic ambient noise data to obtain reliable broad-band surface wave dispersion measurements. *Geophysical Journal International*, *169*(3), 1239–1260. https://doi.org/10.1111/j.1365-246X.2007.03374.x

Ben-Zion, Y., Chen, X., & Zhang, H. (2019). Frontiers in studies of earthquakes and faults: Introduction. *Pure and Applied Geophysics*, *176*(3), 979–982. https://doi.org/10.1007/s00024-019-02139-x

Brocher, T. M. (2005). Empirical relations between elastic wave speeds and density in the Earth's crust. *Bulletin of the Seismological Society of America*, *95*(6), 2081–2092. https://doi.org/10.1785/0120050077

Castellanos, J. C., & Clayton, R. W. (2021). The fine-scale structure of long beach, California, and its impact on ground motion acceleration. *Journal of Geophysical Research: Solid Earth*, *126*(12). https://doi.org/10.1029/2021JB022462

Chen, G., Xu, X., Wen, X., & Wang, Y. (2008). Kinematical transformation and slip partitioning of northern to eastern active boundary belt of Sichuan-Yunnan block [in Chinese]. *Seismology and Geology*, *30*(1), 58–85. https://doi.org/10.3969/j.issn.0253-4967.2008.01.005

Chen, Y., Yu, W., Zhang, H., Yang, B., Li, H., & Ai, H. (2021). Meso-Cenozoic structural deformation and magnetic fabric characteristics of Anninghe fault belt at eastern margin, Tibetan Plateau [in Chinese]. *Journal of Xi'an University of Science and Technology*, *41*(1), 94–103.

Cheng, J., Guo, G., & Yue, Z. (2010). Basic characteristics and earthquake risk analysis of the Anning river fault zone in the west of Sichuan province [in Chinese]. *Journal of Seismological Research*, *33*(3), 265–272.

Cheng, J., Xu, X., Yao, Q., Yang, X., & Chen, H. (2021). Seismic hazard of multi-segment rupturing for the Anninghe-Zemuhe-Daliangshan fault region, southeastern Tibetan Plateau: Constraints from geological and geodetic slip rates. *Natural Hazards*, *107*(2), 1501–1525. https://doi.org/10.1007/s11069-021-04643-7

Fang, H., Yao, H., Zhang, H., Huang, Y. C., & van der Hilst, R. D. (2015). Direct inversion of surface wave dispersion for three-dimensional shallow crustal structure based on ray tracing: Methodology and application. *Geophysical Journal International*, *201*(3), 1251–1263. https://doi.org/10.1093/gji/ggv080

Feng, T., Wu, J., Fang, L., Guo, X., Cai, Y., & Wang, W. (2021). Foreshocks of the 2018 ML 4.0 Shimian earthquake in the Anninghe fault and its implications for earthquake nucleation. *Seismological Research Letters*, *92*(3), 1937–1949. https://doi.org/10.1785/0220200332

Gu, N., Wang, K., Gao, J., Ding, N., Yao, H., & Zhang, H. (2018). Shallow crustal structure of the Tanlu fault zone near Chao Lake in eastern China by direct surface wave tomography from local dense array ambient noise analysis. *Pure and Applied Geophysics*, *176*(3), 1193–1206. https://doi.org/10.1007/s00024-018-2041-4

He, H., & Ikeda, Y. (2007). Faulting on the Anninghe fault zone, southwest China in late quaternary and its movement model [in Chinese]. *Acta Seismologica Sinica*, *29*(5), 537–548.

He, H., Ikeda, Y., He, Y., Togo, M., Chen, J., Chen, C., et al. (2008). Newly-generated Daliangshan fault zone—Shortcutting on the central section of Xianshuihe-Xiaojiang fault system. *Science in China - Series D: Earth Sciences*, *51*(9), 1248–1258. https://doi.org/10.1007/s11430-008-0094-4

Herrmann, R. B. (2013). Computer programs in seismology: An evolving tool for instruction and research. *Seismological Research Letters*, *84*(6), 1081–1088. https://doi.org/10.1785/0220110096

Hu, G., He, Z., Li, N., Ye, T., & Hu, D. (2016). Analyses on integrated geophysical logging results in shallow hole across the Anninghe fault zone [in Chinese]. *Acta Seismologica Sinica*, *38*(5), 684–692.

Hu, Y., & Wang, Z. (2018). Plate interactions, crustal deformation, and magmatism along the eastern margins of the Tibetan Plateau. *Tectonophysics*, *740–741*, 10–26. https://doi.org/10.1016/j.tecto.2018.05.011

Jiang, G., Xu, X., Chen, G., Liu, Y., Fukahata, Y., Wang, H., et al. (2015). Geodetic imaging of potential seismogenic asperities on the Xianshuihe-Anninghe-Zemuhe fault system, southwest China, with a new 3D viscoelastic interseismic coupling model. *Journal of Geophysical Research: Solid Earth*, *120*(3), 1855–1873. https://doi.org/10.1002/2014jb011492

Jin, R., He, X., Fang, H., Xie, J., Liu, Y., & Zhang, P. (2023). Topography effect on ambient noise tomography: A case study for the Longmen Shan area, eastern Tibetan Plateau. *Geophysical Journal International*, *233*(1), 1–12. https://doi.org/10.1093/gji/ggac435

Li, C., Yao, H., Yang, Y., Luo, S., Wang, K., Wan, K., et al. (2020). 3D shear wave velocity structure in the shallow crust of the Tanlu fault zone in Iujiang, Anhui, and adjacent areas, and its tectonic implications. *Earth and Planetary Physics*, *4*(2), 1–12. https://doi.org/10.26464/epp2020026

Li, H., Su, W., Wang, C.-Y., & Huang, Z. (2009). Ambient noise Rayleigh wave tomography in western Sichuan and eastern Tibet. *Earth and Planetary Science Letters*, *282*(1–4), 201–211. https://doi.org/10.1016/j.epsl.2009.03.021

Li, J., Zhou, B., Li, T., Yang, Y., Li, Z., & Long, F. (2020). Seismogenic depths of the Anninghe-Zemuhe and Daliangshan fault zones and their seismic hazards [in Chinese]. *Chinese Journal of Geophysics*, *63*(10), 3669–3682.

Li, Y. C., Hao, M., Song, S., Zhu, L., Cui, D., Zhuang, W., et al. (2021). Interseismic fault slip deficit and coupling distributions on the Anninghe-Zemuhe-Daliangshan-Xiaojiang fault zone, southeastern Tibetan Plateau, based on GPS measurements. *Journal of Asian Earth Sciences*, *219*, 104899. https://doi.org/10.1016/j.jseaes.2021.104899

Li, Y. C., Nocquet, J. M., Shan, X. J., & Jian, H. Z. (2021). Heterogeneous interseismic coupling along the Xianshuihe-Xiaojiang fault system, eastern Tibet. *Journal of Geophysical Research: Solid Earth*, *126*(11). https://doi.org/10.1029/2020JB021187

Lin, F.-C., Moschetti, M. P., & Ritzwoller, M. H. (2008). Surface wave tomography of the western United States from ambient seismic noise: Rayleigh and love wave phase velocity maps. *Geophysical Journal International*, *173*(1), 281–298. https://doi.org/10.1111/j.1365-246X.2008.03720.x

Liu, C., Yao, H., Yang, H., Shen, W., Fang, H., Hu, S., & Qiao, L. (2019b). Direct inversion for three-dimensional shear wave speed azimuthal anisotropy based on surface wave ray tracing: Methodology and application to Yunnan, southwest China. *Journal of Geophysical Research: Solid Earth*, *124*(11), 11394–11413. https://doi.org/10.1029/2018jb016920

Liu, Q. Y., van der Hilst, R. D., Li, Y., Yao, H. J., Chen, J. H., Guo, B., et al. (2014). Eastward expansion of the Tibetan Plateau by crustal flow and strain partitioning across faults. *Nature Geoscience*, *7*(5), 361–365. https://doi.org/10.1038/ngeo2130

Liu, W., Wu, Q., & Zhang, F. (2019). Crustal structure of southeastern Tibetan Plateau inferred from double-difference tomography [in Chinese]. *Acta Seismologica Sinica*, *41*(2), 155–168.

Liu, Y., Yao, H., Zhang, H., & Fang, H. (2021). The community velocity model v.1.0 of southwest China, constructed from joint body- and surface-wave travel-time tomography. *Seismological Research Letters*, *92*(5), 1–16. https://doi.org/10.1785/0220200318

Luo, S., Yao, H., Wang, J., Wang, K., & Liu, B. (2021). Direct inversion of surface wave dispersion data with multiple-grid parametrizations and its application to a dense array in Chao Lake, eastern China. *Geophysical Journal International*, *225*(2), 1432–1452. https://doi.org/10.1093/gji/ggab036

Luo, Y., Xia, J., Miller, R. D., Xu, Y., Liu, J., & Liu, Q. (2008). Rayleigh-wave dispersive energy imaging using a high-resolution linear radon transform. *Pure and Applied Geophysics*, *165*(5), 903–922. https://doi.org/10.1007/s00024-008-0338-4

Luo, Y., Xia, J., Miller, R. D., Xu, Y., Liu, J., & Liu, Q. (2009). Rayleigh-wave mode separation by high-resolution linear radon transform. *Geophysical Journal International*, *179*(1), 254–264. https://doi.org/10.1111/j.1365-246X.2009.04277.x

Mordret, A., Roux, P., Boué, P., & Ben-Zion, Y. (2019). Shallow three-dimensional structure of the San Jacinto fault zone revealed from ambient noise imaging with a dense seismic array. *Geophysical Journal International*, *216*(2), 896–905. https://doi.org/10.1093/gji/ggy464

Ran, Y., Chen, L., Cheng, J., & Gong, H. (2008). Late quaternary surface deformation and rupture behavior of strong earthquake on the segment north of Mianning of the Anninghe fault. *Science in China - Series D: Earth Sciences*, *51*(9), 1224–1237. https://doi.org/10.1007/s11430-008-0104-6

Rawlinson, N., & Sambridge, M. (2005). The fast marching method: An effective tool for tomographic imaging and tracking multiple phases in complex layered media. *Exploration Geophysics*, *36*(4), 341–350. https://doi.org/10.1071/eg05341

Rawlinson, N., & Spakman, W. (2016). On the use of sensitivity tests in seismic tomography. *Geophysical Journal International*, *205*(2), 1221–1243. https://doi.org/10.1093/gji/ggw084

Ren, Z. (2014). Late quaternary deformation features along the Anninghe fault on the eastern margin of the Tibetan Plateau. *Journal of Asian Earth Sciences*, *85*, 53–65. https://doi.org/10.1016/j.jseaes.2014.01.025

Royden, L. H., Burchfiel, B. C., King, R. W., Wang, E., Chen, Z., Shen, F., & Liu, Y. (1997). Surface deformation and lower crustal flow in eastern Tibet. *Science*, *276*(5313), 788–790. https://doi.org/10.1126/science.276.5313.788

Schoenbohm, L. M., Burchfiel, B. C., & Liangzhong, C. (2006). Propagation of surface uplift, lower crustal flow, and Cenozoic tectonics of the southeast margin of the Tibetan Plateau. *Geology*, *34*(10), 813–816. https://doi.org/10.1130/g22679.1

SGBMG. (1967). Regional geological survey report (Mianning, h4831, geological part). [Online Database] Retrieved from http://www.ngac.org.cn/map/document?guid=ec7e1a7a754f1954e0430100007f182e

Shao, X., Yao, H., Liu, Y., Yang, H., Tian, B., & Fang, L. (2022). Shallow crustal velocity structures revealed by active source tomography and fault activities of the Mianning-Xichang segment of the Anninghe fault zone, SW China. *Earth and Planetary Physics*, *6*. https://doi.org/10.26464/epp2022010

Shen, Y., Ren, Y., Gao, H., & Savage, B. (2012). An improved method to extract very-broadband empirical green's functions from ambient seismic noise. *Bulletin of the Seismological Society of America*, *102*(4), 1872–1877. https://doi.org/10.1785/0120120023

Su, G., Tian, X., Sun, Q., Deng, D., Chang, L., & Wang, S. (2017). Research on vertical deformation and fault activity of Sichuan-Yunnan area [in Chinese]. *Journal of Geodesy and Geodynamics*, *37*(7), 686–691.

Tapponnier, P., Peltzer, G., Le Dain, A. Y., Armijo, R., & Cobbold, P. (1982). Propagating extrusion tectonics in Asia: New insights from simple experiments with plasticine. *Geology*, *10*(12), 611–616. https://doi.org/10.1130/0091-7613(1982)10⟨611:Petian⟩2.0.Co;2

Tian, X., Zhan, W., Zheng, H., & Yin, H. (2021). Characteristics of present-day 3D crustal movement of Sichuan-Yunnan region [in Chinese]. *Journal of Geodesy and Geodynamics*, *41*(7), 739–746.

Trad, D., Ulrych, T., & Sacchi, M. (2003). Latest views of the sparse radon transform. *Geophysics*, *68*(1), 386–399. https://doi.org/10.1190/1.1543224

Tromp, J., Komatitsch, D., & Liu, Q. (2008). Spectral-element and adjoint methods in seismology. *Communications in Computational Physics*, *3*(1), 1–32.

Turner, G. (1990). Aliasing in the tau-*p* transform and the removal of spatially aliased coherent noise. *Geophysics*, *55*(11), 1496–1503. https://doi.org/10.1190/1.1442797

Wan, Z., Zhao, G., Tang, J., Chen, X., Wang, L., Xiao, Q., et al. (2010). The electrical structure of the crust along Mianning-Yibin profile in the eastern edge of Tibetan Plateau and its tectonic implications [in Chinese]. *Chinese Journal of Geophysics*, *53*(3), 585–594.

Wang, H., Ran, Y., Chen, L., Liang, M., Gao, S., Li, Y., & Xu, L. (2018). Determination of slip rate on the southern segment of the Anninghe fault [in Chinese]. *Seismology and Geology*, *40*(5), 967–979.

Wang, H., Ran, Y., Li, Y., & Chen, L. (2014). Paleoseismic behavior of the Anninghe fault and its comparison with the Zemuhe fault in western Sichuan [in Chinese]. *Seismology and Geology*, *36*(3), 706–717.

Wang, H., Ran, Y., Li, Y., Gomez, F., & Chen, L. (2014). A 3,400 yr long paleoseismologic record of earthquakes on the southern segment of Anninghe fault on the southeastern margin of the Tibetan Plateau. *Tectonophysics*, *628*, 206–217. https://doi.org/10.1016/j.tecto.2014.04.040

Wang, Q., Xu, X., & Jiang, Z. (2020). Strain characteristics of north-south seismic zone and the analysis of earthquake risk [in Chinese]. *Journal of Geodensy and Geodynamics*, *40*(1), 23–29.

Wang, Q., Zhang, P. Z., Freymueller, J. T., Bilham, R., Larson, K. M., Lai, X., et al. (2001). Present-day crustal deformation in China constrained by global positioning system measurements. *Science*, *294*(5542), 574–577. https://doi.org/10.1126/science.1063647

Wang, W., Gerstoft, P., & Wang, B. (2018). Interference of teleseismic body waves in noise cross-correlation functions in southwest China. *Seismological Research Letters*, *89*(5), 1817–1825. https://doi.org/10.1785/0220180139

Wang, W., Wu, J., Fang, L., Lai, G., & Cai, Y. (2017). Crustal thickness and Poisson's ratio in southwest China based on data from dense seismic arrays. *Journal of Geophysical Research: Solid Earth*, *122*(9), 7219–7235. https://doi.org/10.1002/2017jb013978

Wang, Z., Su, J., Liu, C., & Cai, X. (2015). New insights into the generation of the 2013 Lushan earthquake (M_s7.0), China. *Journal of Geophysical Research: Solid Earth*, *120*(5), 3507–3526. https://doi.org/10.1002/2014jb011692

Wen, X. Z., Fan, J., Yi, G. X., Deng, Y. W., & Long, F. (2008). A seismic gap on the Anninghe fault in western Sichuan, China. *Science in China - Series D: Earth Sciences*, *51*(10), 1375–1387. https://doi.org/10.1007/s11430-008-0114-4

Wessel, P., Smith, W. H. F., Scharroo, R., Luis, J., & Wobbe, F. (2013). Generic mapping tools: Improved version released. *Eos, Transactions American Geophysical Union*, *94*(45), 409–410. https://doi.org/10.1002/2013eo450001

Wirth, E. A., Vidale, J. E., Frankel, A. D., Pratt, T. L., Marafi, N. A., Thompson, M., & Stephenson, W. J. (2019). Source-dependent amplification of earthquake ground motions in deep sedimentary basins. *Geophysical Research Letters*, *46*(12), 6443–6450. https://doi.org/10.1029/2019gl082474

Yang, H. F., Duan, Y. H., Song, J. H., Jiang, X. H., Tian, X. F., Yang, W., et al. (2020). Fine structure of the Chenghai fault zone, Yunnan, China, constrained from teleseismic travel time and ambient noise tomography. *Journal of Geophysical Research: Solid Earth*, *125*(7). https://doi.org/10.1029/2020JB019565

Yang, H. F., Duan, Y., Song, J. H., Wang, W., Yang, W., Tian, X., & Wang, B. (2021). Illuminating high-resolution crustal fault zones using multi-scale dense arrays and airgun source. *Earthquake Research Advances*, *1*(1), 100001. https://doi.org/10.1016/j.eqrea.2021.100001

Yang, Y., Li, Y., Guan, Z., Chen, Z., Zhang, L., Lv, C. J., & Sun, F. (2018). Correlations between the radon concentrations in soil gas and the activity of the Anninghe and the Zemuhe faults in Sichuan, southwestern of China. *Applied Geochemistry*, *89*, 23–33. https://doi.org/10.1016/j.apgeochem.2017.11.006

Yang, Y., Li, Y., Li, Y., Ji, L., Gong, Y., Du, F., et al. (2021). Present-day activity of the Anninghe fault and Zemuhe fault, southeastern Tibetan Plateau, derived from soil gas CO_2 emissions and locking degree. *Earth and Space Science*, *8*(10). https://doi.org/10.1029/2020ea001607

Yang, Z., Wang, F., Duan, Y., Zhang, C., Zhao, J., Zhang, J., & Liu, B. (2011). Basement structure of southeastern boundary region of Sichuan-Yunnan active block: Analysis results of Yanyuan-Xichang-Zhaojue-Mahu deep seismic sounding profile [in Chinese]. *Acta Seismologica Sinica*, *33*(4), 431–442.

Yao, H. (2020). Building the community velocity model in the Sichuan-Yunnan region, China: Strategies and progresses. *Science China Earth Sciences*, *63*(9), 1425–1428. https://doi.org/10.1007/s11430-020-9645-3

Yao, H., Gouédard, P., Collins, J. A., McGuire, J. J., & van der Hilst, R. D. (2011). Structure of young east Pacific rise lithosphere from ambient noise correlation analysis of fundamental- and higher-mode Scholte-Rayleigh waves. *Comptes Rendus Geoscience*, *343*(8–9), 571–583. https://doi.org/10.1016/j.crte.2011.04.004

Yao, H., van der Hilst, R. D., & de Hoop, M. V. (2006). Surface-wave array tomography in SE Tibet from ambient seismic noise and two-station analysis—I. Phase velocity maps. *Geophysical Journal International*, *166*(2), 732–744. https://doi.org/10.1111/j.1365-246X.2006.03028.x

Yao, S., & Yang, H. (2022). Hypocentral dependent shallow slip distribution and rupture extents along a strike-slip fault. *Earth and Planetary Science Letters*, *578*, 117296. https://doi.org/10.1016/j.epsl.2021.117296

Yi, G., Wen, X., & Su, Y. (2008). Study on the potential strong-earthquake risk for the eastern boundary of the Sichuan-Yunnan active faulted-block [in Chinese]. *Chinese Journal of Geophysics*, *51*(6), 1719–1725.

Zhang, W., & Chen, X. (2006). Traction image method for irregular free surface boundaries in finite difference seismic wave simulation. *Geophysical Journal International*, *167*(1), 337–353. https://doi.org/10.1111/j.1365-246X.2006.03113.x

Zhang, Y., Li, H., & Li, J. (2010). Middle Pleistocene extension along the eastern margin of Xizang (Tibetan) Plateau and its neotectonic significance [in Chinese]. *Geological Review*, *56*(6), 781–791.

Zhang, Y., Yao, H., Yang, H.-Y., Cai, H.-T., Fang, H., Xu, J., et al. (2018). 3D crustal shear-wave velocity structure of the Taiwan Strait and Fujian, SE China, revealed by ambient noise tomography. *Journal of Geophysical Research: Solid Earth*, *123*(9), 8016–8031. https://doi.org/10.1029/2018jb015938

Zhang, Z., Yao, H., & Yang, Y. (2020). Shear wave velocity structure of the crust and upper mantle in southeastern Tibet and its geodynamic implications. *Science China Earth Sciences*, *63*(9), 1278–1293. https://doi.org/10.1007/s11430-020-9625-3

Zhang, Z., Zhang, W., & Chen, X. (2014). Three-dimensional curved grid finite-difference modeling for non-planar rupture dynamics. *Geophysical Journal International*, *199*(2), 860–879. https://doi.org/10.1093/gji/ggu308

Zhao, B., Huang, Y., Zhang, C., Wang, W., Tan, K., & Du, R. (2015). Crustal deformation on the Chinese mainland during 1998–2014 based on GPS data. *Geodesy and Geodynamics*, *6*(1), 7–15. https://doi.org/10.1016/j.geog.2014.12.006

Zhu, S., Yang, G., Liu, X., & Dang, X. (2017). The deformation characteristics of Sichuan-Yunnan region in recent period [in Chinese]. *Geomatics and Information Science of Wuhan University*, *42*(12), 1765–1772.